

Deep and rapid observations of strong-lensing galaxy clusters within the sky localisation of GW170814

G. P. Smith,^{1*} M. Bianconi,¹ M. Jauzac,^{2,3,4} J. Richard,⁵ A. Robertson,³
 C. P. L. Berry,^{1,6} R. Massey,² K. Sharon,⁷ W. M. Farr,^{1,6} J. Veitch⁸

¹ School of Physics and Astronomy, University of Birmingham, Birmingham, B15 2TT, England

² Centre for Extragalactic Astronomy, Department of Physics, Durham University, Durham DH1 3LE, England

³ Institute for Computational Cosmology, Durham University, South Road, Durham DH1 3LE, England

⁴ Astrophysics and Cosmology Research Unit, School of Mathematical Sciences, University of KwaZulu-Natal, Durban 4041, South Africa

⁵ Univ Lyon, Univ Lyon1, Ens de Lyon, CNRS, Centre de Recherche Astrophysique de Lyon UMR5574, F-69230, Saint-Genis-Laval, France

⁶ Institute of Gravitational Wave Astronomy, University of Birmingham, Birmingham, B15 2TT, England

⁷ Department of Astronomy, University of Michigan, 1085 S. University Avenue, Ann Arbor, MI 48109, USA

⁸ School of Physics and Astronomy, University of Glasgow, G12 8QQ, Scotland

15 June 2022

ABSTRACT

We present observations of two strong-lensing galaxy clusters located within the 90 per cent credible sky localization released following LIGO-Virgo’s discovery of the binary black hole (BBH) source GW170814. Our objectives were (1) to search for candidate electromagnetic (EM) counterparts to this source under the hypothesis that it was strongly-lensed and thus more distant and less massive than inferred by LIGO-Virgo, and (2) to demonstrate the feasibility of rapid target of opportunity observations to search for faint lensed transient point sources in crowded cluster cores located within GW sky localizations. Commencing 20 hours after discovery, and continuing over 12 nights, we observed Abell 3084 ($z = 0.22$) and SMACS J0304.3–4401 ($z = 0.46$) with GMOS on the Gemini-South telescope, and Abell 3084 with MUSE on ESO’s Very Large Telescope. Careful analysis, and calibration of our methods using simulations, yield 5σ detection limits on transients in difference images of the cores of these clusters of 25th magnitude for continuum emission, and $5 \times 10^{-17} \text{ erg s}^{-1} \text{ cm}^{-2}$ for line emission. This is the first emission-line search for optical counterparts to GW sources, and the most sensitive continuum search to date – we reach an apparent magnitude limit before correction for lens magnification that is $\gtrsim 2$ magnitudes fainter than previous searches. Moreover, we show that the lens magnification suffered by GW sources cancels the inverse square law, and therefore our observations are uniformly sensitive to lensed sources across the full range of redshifts at which stellar-mass binary compact objects are credible LIGO-Virgo sources.

Key words: galaxies: clusters: individual Abell 3084, SMACS J0304.3–4401 — gravitational lensing: strong — gravitational waves

1 INTRODUCTION

Observational astronomy gained a new tool with the first direct detection of gravitational waves (GWs; Abbott et al. 2016c). GWs have already provided new insights in to the properties of compact binaries and the nature of gravity (e.g., Abbott et al. 2016a,f; Abbott et al. 2017) that complement those accessible by electromagnetic observations. In

the case of GW170817 (Abbott et al. 2017e), the first GW signal from a binary neutron star (BNS) coalescence, was followed by observations of a counterpart across the electromagnetic (EM) spectrum (Abbott et al. 2017f). These multi-messenger observations permitted new tests of general relativity (Abbott et al. 2017b), measurement of the Hubble constant (Abbott et al. 2017a), and information on neutron star physics (e.g., Abbott et al. 2017g; Levan et al. 2017; Margalit & Metzger 2017; Bauswein et al. 2017).

* E-mail: gps@star.sr.bham.ac.uk

Optical follow-up observations of stellar-mass compact

binary coalescence (CBC) sources of GWs rely on the three-dimensional localization of the source from the LIGO-Virgo data. The sky location and its uncertainties guide the observability with a given telescope and where on the celestial sphere to point it; the luminosity distance and the luminosity of plausible optical counterparts guide how long to observe. With only two GW detectors, sky localizations can be $\sim 100\text{--}1000\text{ deg}^2$ (Singer et al. 2014; Berry et al. 2015); adding additional detectors to the network improves sky localization (Veitch et al. 2012; Abbott et al. 2016e; Pankow et al. 2018) and enhances three-dimensional localization (Singer et al. 2016; Del Pozzo et al. 2018). Towards the end of LIGO-Virgo’s second observing run (O2) in 2017, when all three detectors were operational, the sky localizations from LIGO and Virgo for their loud (signal-to-noise ratio ≥ 18) GW detections were $\sim 30\text{--}60\text{ deg}^2$ (Abbott et al. 2017d,e).

The largest cameras on 4-m and 8-m class optical/near-infrared telescopes have fields of view of up to a few square degrees. It is therefore time consuming to search thoroughly the error regions of even these best localized GW sources, especially in the case of binary black hole (BBH) mergers, for which any EM counterparts are expected to be faint or non-existent. For example, using GW170817 as a guide to the luminosity of a kilonova-like EM counterpart ($M \simeq -13.5$; e.g., Arcavi 2018), and thus upper limit to the brightness of an EM counterpart to a BBH merger, suggests that any EM counterpart to a BBH source that has been detected at $D_L \gtrsim 300\text{ Mpc}$ will have an apparent magnitude of $m \gtrsim 24$. To date, strategies designed to overcome the challenges inherent in the large sky localization uncertainties include optimizing the tiling and scheduling of wide-field searches (Coughlin et al. 2018), and targeting the follow-up observations on stellar mass selected galaxies located within the three-dimensional GW localizations (Nissanke, Kasliwal & Georgieva 2013; Hanna, Mandel & Vuisden 2014; Gehrels et al. 2016). The latter approach was deployed to great success in the earliest identification of the optical counterpart to the BNS signal GW170817 (Coulter et al. 2017).

The luminosity distance to CBC sources is measured to 30–40 per cent precision from LIGO-Virgo data (Berry et al. 2015; Abbott et al. 2016b; Abbott et al. 2017; Abbott et al. 2017c,d,e). Gravitational lensing, and in particular strong lensing, is a possible source of systematic bias in these inferred luminosity distances. This is because the amplitude of the strain signal A depends on both lens magnification μ , and luminosity distance D_L : $A \propto |\mu|^{0.5} D_L^{-1}$ (hereafter we use μ to denote $|\mu|$). Therefore lens magnification allows sources from greater distances to be observed, and also means that the luminosity distance to a lensed source inferred assuming $\mu = 1$ is under-estimated by a factor $\mu^{0.5}$. The systematic bias in the inferred distance also means that the masses of the source, which are calculated using the inferred source redshift (Krolak & Schutz 1987), are over-estimated by a factor $(1 + z_{\mu=1})/(1 + z)$, where $z_{\mu=1}$ is the redshift inferred assuming $\mu = 1$, and z is the true redshift of the lensed source. Therefore, while lensing does complicate the measurement of distance, identification of a lensed source with LIGO-Virgo would provide a glimpse of the CBC population at $z \gtrsim 1$, well in advance of third-generation GW detectors.

A strongly-lensed GW would travel to Earth along mul-

iple paths of least action through the foreground mass concentration, and thus in principle could be detected on more than one occasion by LIGO-Virgo, as would any EM counterpart. These paths differ in length, leading to a time delay between detections of consecutive signals in the range $t_{\text{delay}} \simeq 1\text{--}100$ days (Smith et al. 2018). Multiple detections of a single CBC source, coupled with the sub-millisecond precision to which the arrival time of GW signals are measured by LIGO-Virgo (Abbott et al. 2016d,b; Abbott et al. 2017), would create unique scientific opportunities. The measured precision on the time delay between the arrival of lensed GW signals is $\gtrsim 8$ orders of magnitude superior to that achievable with supernovae or quasars (e.g., Fohlmeister et al. 2007; Rodney et al. 2016). Therefore, we could obtain unprecedented constraints on the distribution of dark and luminous matter in the gravitational lens, and a new and highly accurate measurement of the Hubble parameter (Liao et al. 2017). Multiple detections of the same GW source should also enable new constraints on GW polarizations, because the number of detectors that would observe the same GW signal would grow with the multiplicity of the strongly-lensed event (cf. Chatziioannou, Yunes & Cornish 2012).

The probability of a GW source detected to date with LIGO-Virgo being strongly-lensed is small, but non-zero, due to the lens magnifications of $\mu \simeq 100$ that are required (Smith et al. 2018). Such large lens magnification helps to clarify that, based on observations and theoretical predictions to date, galaxy clusters and groups ($M_{\text{halo}} > 10^{13} M_{\odot}$; hereafter clusters) are the relevant gravitational lenses for strong-lensing of GWs (for an alternative point of view, see: Broadhurst, Diego & Smoot 2018; Li et al. 2018; Ng et al. 2018). This is because GW sources can be treated as point sources, and both observations (Oguri 2010; Oguri et al. 2013; Inada et al. 2014; Sharon et al. 2017) and predictions (Figure 5 from Hilbert et al. 2008) currently point to the optical depth to high magnification strong-lensing of point sources being dominated by galaxy clusters.

From the LIGO-Virgo signal alone, it would be difficult to identify that a GW source is strongly-lensed. This is because the over-estimated mass of the compact objects may not appear anomalous, and the GW sky localization uncertainties dwarf the solid angle subtended by strong-lensing cluster cores ($\sim 1\text{--}2\text{ arcmin}^2$) by ~ 5 orders of magnitude. Therefore, strong evidence beyond that available from the strain signal measured by LIGO-Virgo would be needed to outweigh the low prior expectation that a given GW signal was strongly-lensed. Identification of an EM counterpart to a GW source in the core of a strong-lensing cluster, and detection of a subsequent image of the same source would provide such evidence, and thus establish that a GW had been strongly-lensed. This would allow the correct source parameters to be inferred, and enable the science outlined above.

In this article we introduce a new observing strategy for identifying optical counterparts to GW sources – observations of strong-lensing galaxy cluster cores located within LIGO-Virgo GW sky localizations. We describe our first implementation of this strategy via rapid target of opportunity

(ToO) observations with the Gemini-South telescope¹ and ESO’s Very Large Telescope² (VLT) in the nights immediately following the discovery of the BBH source GW170814 (Abbott et al. 2017d). Our observations targeted known strong-lensing galaxy clusters, selected from the list compiled by Smith et al. (2018). The main goals of our observations were to test the feasibility of searching for optical transients in rapid follow-up observations with small field-of-view instruments (that are well matched to cluster cores, and not routinely used for discovery of transient objects) on 8-m class telescopes, and to actually search in earnest for candidate EM counterparts to putative strongly-lensed GW sources. The large aperture of Gemini-South and VLT, and the absence of any requirement for us to explore the wider sky localization, enabled us to conduct deep observations that are sensitive to strongly-lensed EM counterparts down to $m = 25$ independent of the actual source redshift. Our strategy therefore benefits from greater sensitivity than conventional searches, at the expense of a much smaller survey volume.

We describe the details of our observing strategy, observations, and data reduction in Section 2, explain how we generate difference images, and search for candidate optical counterparts, and state our results in Section 3, discuss our results in Section 4, and summarize the key points in Section 5. We assume a flat cosmology with $H_0 = 67.9 \text{ km s}^{-1} \text{ Mpc}^{-1}$, $\Omega_M = 0.3065$ (Ade et al. 2016). All celestial coordinates are stated at the J2000 epoch, and all magnitudes are stated in the AB system.

2 OBSERVATIONS

2.1 Observing strategy

We aim to conduct the most sensitive search to date for optical emission from CBC sources of GWs, under the hypothesis that the objects that we target have been strongly-lensed by a massive foreground galaxy cluster. We therefore select known, spectroscopically-confirmed strong-lensing clusters located close to the peak probability of the sky localization maps of LIGO Scientific-Virgo Collaboration (LVC) CBC alerts. The strong-lensing regions of these clusters span $\sim 1\text{--}2 \text{ arcmin}^2$ on the sky, and are thus perfectly matched to instruments on ground-based 8-m class telescopes, including the GMOS instruments on the Gemini-North and South telescopes, and MUSE on VLT.

The most common GW sources are the coalescence of BBHs. Optical emission from BBHs is expected to be faint or non-existent (Abbott et al. 2016e, and references therein). Searches for optical emission from BBH mergers have typically reached sensitivity limits of $m \lesssim 22$ with telescopes up

to 4-m in diameter and $m \simeq 22\text{--}24$ with the Subaru 8-m telescope (e.g., Soares-Santos et al. 2016; Cowperthwaite et al. 2016; Yoshida et al. 2017; Arcavi et al. 2017; Utsumi et al. 2018). We therefore adopted a nominal goal of reaching a spectral flux density limit with GMOS and MUSE corresponding to $m \simeq 25$, in order to push the sensitivity of EM follow-up observations in to a new regime independent of any lens magnification. After taking account of lens magnification of (say) $\mu \simeq 100$, this translates to a search for optical emission from BBHs down to $m \simeq 25 + 2.5 \log(\mu) = 30$.

Our observations are guided by the best localizations provided by the LVC at the time. Localizations are refined as improved analyses become available (Abbott et al. 2016e), but since we expect an optical counterpart to fade rapidly, it is not possible to delay follow-up observations until final localizations are communicated. We identify the clusters for potential observations by comparing the celestial coordinates of 130 strong-lensing clusters selected by Smith et al. (2018) with the LVC sky localization. We use the two-dimensional sky localization to prioritize the most promising observing targets. Typically, we pick the strong-lensing cluster closest to the peak of the probability distribution as the most promising to observe.

Our ToO observing programmes at the Gemini Observatory and European Southern Observatory (hereafter ESO) commenced in early August 2017 under programme IDs GN-2017A-DD-9, GS-2017A-DD-6, 299.A-5028 respectively. These programmes allowed for up to 7 epochs of imaging observations with the GMOS instruments on the Gemini-North and Gemini-South telescopes, and up to 3 epochs of integral field spectroscopy with MUSE on VLT. The observations commence as soon as possible after receipt of the LVC alert via a rapid ToO, and were planned to extend over a period of one week following the alert via regular ToO observations.

2.2 Identification of strong-lensing clusters in the GW170814 sky localization

GW170814 was detected by LIGO and Virgo on August 14, 2017 at 10:30:43 UTC, and first announced via GCN circular on August 14, 2017 at 12:28:42 UTC (LIGO Scientific Collaboration and Virgo Collaboration 2017a) with an initial false alarm rate of ~ 1 in 80,000 years. The 90 per cent credible region in the initial BAYESTAR (Singer & Price 2016) sky localization map spanned 97 deg^2 , centered at celestial coordinates of $(\alpha, \delta) = (02:44:00, -45:29:00)$. We identified one strong-lensing cluster within the 90 per cent credible region of the BAYESTAR map. Abell 3084, at a redshift of $z = 0.22$ and celestial coordinates $(\alpha, \delta) = (03:04:07, -36:56:36)$, lies on the contour encircling a region within which the sky localization probability is $p = 0.8$, and which subtends 57.5 deg^2 (Figure 1).

As the LVC analyses were refined, the localization region evolved (Figure 1). On August 16, 2017 at 07:02:19 UTC, the sky localization was updated based on the results of LALINFERENCE (Veitch et al. 2015), with a revised centre close to celestial coordinates of $(\alpha, \delta) = (03:06:00, -44:36:00)$ and a 90 per cent credible region spanning 190 deg^2 (LIGO Scientific Collaboration and Virgo Collaboration 2017b). We identified two strong-lensing clusters within the 90 per cent credible region of the LALINFERENCE map. Abell 3084 lay on the contour encircling $p = 0.873$ per

¹ Based on observations obtained at the Gemini Observatory, which is operated by the Association of Universities for Research in Astronomy, Inc., under a cooperative agreement with the NSF on behalf of the Gemini partnership: the National Science Foundation (United States), the National Research Council (Canada), CONICYT (Chile), Ministerio de Ciencia, Tecnología e Innovación Productiva (Argentina), and Ministério da Ciência, Tecnologia e Inovação (Brazil).

² Based on observations made with ESO Telescopes at the La Silla Paranal Observatory under programme ID 299.A-5028.

cent of the localization probability density, corresponding to a region subtending 154.4 deg^2 – i.e. this cluster is further from the peak of the probability distribution following the update. SMACS J0304.3–4401 at $z = 0.46$ with celestial coordinates $(\alpha, \delta) = (03:04:21, -44:01:48)$, lies closer to the peak of the probability distribution, on the contour which encloses $p = 0.05$ of the sky localization probability and subtends 2.1 deg^2 .

The final sky localization of GW170814 was centred at $(\alpha, \delta) = (03:11:00, -44:57:00)$, with a 90 per cent credible region spanning 60 deg^2 , and a revised luminosity distance of $D_L = 540_{-210}^{+130} \text{ Mpc}$ (Abbott et al. 2017d). With this, Abell 3084 lay on the $p = 0.994$ contour that subtends 170.4 deg^2 , and SMACS J0304.3–4401 lay on the $p = 0.568$ contour that subtends 16.1 deg^2 .

2.3 Abell 3084 and SMACS J0304.3–4401

Detailed models of the mass distribution in the core of Abell 3084 and SMACS J0304.3–4401 (May 2013, Christensen et al. 2012) are vital to interpreting the sensitivity of our observations and any flux that we detect from a candidate EM counterpart. Each model is constrained by spectroscopically confirmed multiple images detected in each cluster core. The model of Abell 3084 is constrained by a 5-image system at $z_S = 0.764$, and the model of SMACS J0304.3–4401 is constrained by a 3-image system at $z_S = 1.963$. The models are therefore most accurate for these source redshifts, and we concentrate on these redshifts when considering the efficiency of our search for candidate EM counterparts in Section 3. *Hubble Space Telescope (HST)* snapshot observations with the Advanced Camera for Surveys (ACS) are available for both clusters, through the F606W filter (PID: 10881 and 12166). We use these data to calibrate our GMOS and MUSE observations (Sections 2.5 & 2.6) and in our difference image analysis (Section 3.1).

2.4 Gemini and VLT observations

We observed Abell 3084 with GMOS on Gemini-S on five occasions, commencing 20 hours after the first LVC alert pertaining to GW170814, on August 15, 2017 UTC. This was the first Chilean night following the detection of GW170814. The GMOS observations of Abell 3084 continued after the revised sky map became available, in order to obtain a comprehensive dataset on one cluster. We also observed SMACS J0304.3–4401 with GMOS on Gemini-S on two occasions – August 18 and 21. The overall aim was to observe for ~ 45 minutes on each night, with the exposure times and number of exposures adjusted to suit the Moon phase and overhead conditions. The individual exposures were offset from each other randomly within a square region of full width 30 arcsec . Observations were performed in the i -band in order to minimize the impact of the Moon on the sensitivity of the observations, and to probe rest-frame V -band emission from putative lensed GWs at $z \gtrsim 0.5$.

We triggered a rapid ToO on VLT with MUSE within 3 hours after LVC announced the detection of GW170814. This observation was executed at the telescope on August 17, 2017 UTC, and repeated on August 20, 2017 UTC. The

delay between our trigger and the first MUSE observation was due to a combination of visitor mode time and engineering time on the intervening nights. Each observation comprised three exposures of duration 980 s and spanned the wavelength range $475 < \lambda < 930 \text{ nm}$.

All of the GMOS and MUSE data were obtained at high elevation and with excellent seeing of $0.5 \leq \text{FWHM} \leq 1 \text{ arcsec}$. Details of the GMOS and MUSE observations are listed in Table 1, and the reduction of GMOS and MUSE data is described in Sections 2.5 & 2.6 respectively.

2.5 GMOS data reduction

Individual GMOS exposures were de-biased, dark-subtracted, flat-fielded, and sky-subtracted in the standard manner using the GEMINI package in IRAF, to produce both a single science frame comprising the mosaiced individual chips, and a bad-pixel map, for each exposure. The bad-pixel maps were applied to the science frames and the individual masked science frames were then combined in to a single stacked frame per visit using the IMCOMBINE task in IRAF. The full width at half maximum of point sources in the reduced frames is consistently sub-arcsecond (Table 1). The reduced and stacked frames were aligned with the first visit for that target to a typical root-mean-square residual accuracy of 0.03 pixels using the IRAF tasks GEOMAP and GEOTRAN.

We searched the available USNO and GSC catalogues for sources of well calibrated i -band magnitude within the field of view of our GMOS data. The size and depth of the GMOS imaging even in short exposures meant that there was no overlap between unsaturated bright stars as seen by Gemini and faint stars measured in all-sky surveys. We therefore calibrated the GMOS frames by measuring the $(V_{606} - i)$ colours of sources detected in both the archival *HST*/ACS data and our GMOS data, and selecting the photometric zero point that yields the correct colours for massive early-type galaxies in Abell 3084 and SMACS J0304.3–4401 respectively. These colours were computed using the EZGAL code,³ based on a single stellar population that formed at high redshift and evolved passively to the relevant cluster redshifts based on the Bruzual & Charlot (2003) population synthesis code. The predicted colours are insensitive to the fine details of how we choose the formation redshift and the metallicity. We show an example $(V_{606} - i)/i$ colour-magnitude diagram for one of the observations of Abell 3084 in Figure 2.

2.6 MUSE data reduction

The MUSE observations were reduced using version 2.0 of the data reduction software (Weilbacher et al. 2014). The process includes basic calibration (bias removal, flat-fielding, wavelength and geometrical calibration) and the production of datacubes for each exposure following sky subtraction, flux calibration and telluric correction. These datacubes were matched in astrometry to the relevant *HST* observation discussed in Section 2.3. In all cases, only a constant offset in right ascension and declination was applied, as no

³ www.baryons.org/ezgal/

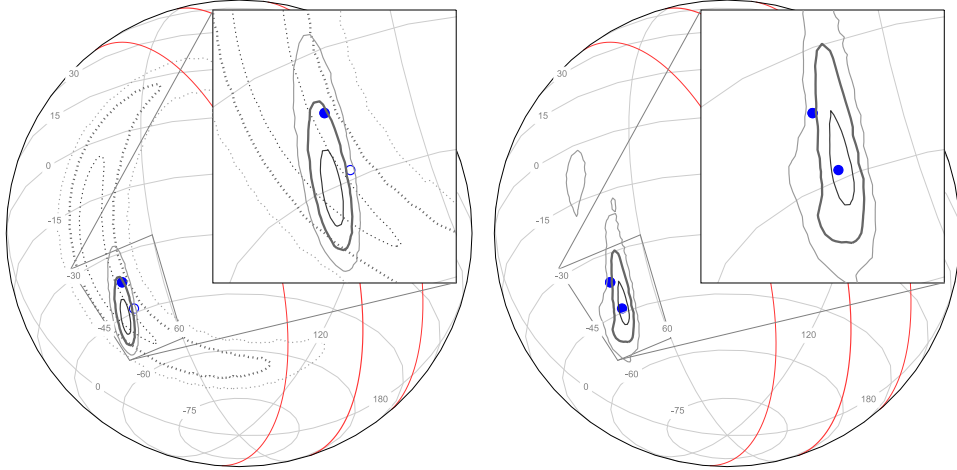


Figure 1. LEFT – Initial BAYESTAR skymap for GW170814 from GCN 21474, showing the LIGO only contours (dotted), joint LIGO-Virgo contours (solid), Abell 3084 (filled blue), and SMACS J0304.3–4401 (open blue). RIGHT – Initial LALINFERENCE skymap from GCN 21493, showing updated sky localisation based on LIGO-Virgo data (solid) and the locations of both clusters. SMACS J0304.3–4401 is closer to the peak of the sky localisation than Abell 3084 in the revised map. In both panels the 90 per cent credible region is shown as the thick solid contour, and galactic latitudes of $\pm 20^\circ$ are shown in red.

Table 1. Follow-up observations of strong-lensing clusters within sky localisation of GW170814

Visit	Start of observation (UTC)	Airmass ^a	Integration time (ks)	Seeing ^b (arcsec)	Sensitivity ^c
GMOS OBSERVATIONS OF ABELL 3084					
1	August 15, 2017, 06:40:40	1.29	2.9	0.72	24.7
2	August 17, 2017, 07:50:52	1.09	2.3	0.49	25.2
3	August 18, 2017, 06:14:13	1.33	3.1	0.81	24.8
4	August 21, 2017, 07:09:38	1.05	3.1	0.76	24.9
5	August 28, 2017, 07:44:48	1.03	3.1	0.84	24.9
GMOS OBSERVATIONS OF SMACS J0304.3–4401					
1	August 18, 2017, 07:23:35	1.14	2.3	1.01	24.9
2	August 21, 2017, 05:58:47	1.35	3.1	0.88	25.1
3	August 27, 2017, 08:02:50	1.04	2.9	0.97	25.0
MUSE OBSERVATIONS OF ABELL 3084					
1	August 17, 2017, 08:02:13	1.10	2.9	0.85	25.8
2	August 19, 2017, 07:46:50	1.12	2.9	0.82	25.9

^a The airmass at the mid-point of the observation.

^b Mean full width at half maximum of point sources in the reduced data, with a typical error on the mean of ~ 0.02 arcsec.

^c 5σ point source sensitivity within a photometric aperture of diameter 2 arcsec, estimated from the magnitude at which the median photometric uncertainty is 0.2 magnitudes. The sensitivity of the MUSE observations is stated in the F606W-band.

significant rotation was found. The measured offsets and rotation were applied back to the original list of pixels (the so-called pixel table) so that the datacubes can be produced in a single interpolation step to limit the effect on the noise properties. Each exposure datacube was treated for sky subtraction residuals using the PCA method implemented in the ZAP v2.0 software (Soto et al. 2016). We then combined all zapped exposures taken during each of the two observations.

We assessed the image quality of the MUSE observations by performing a Moffat spatial fit of the bright un-

saturated stars in each exposure. The seeing was stable in each night with average values provided in Table 1. We also estimated the cloud extinction to be just a few per cent and thus negligible, based on a comparison between MUSE pseudo-F606W frames (see Section 3.1) and relevant *HST* frames.

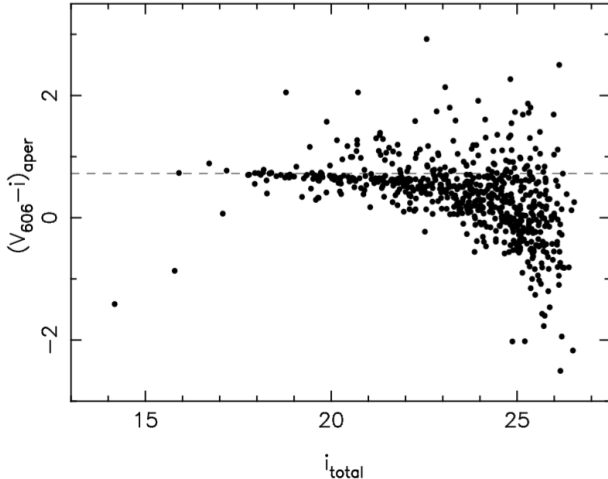


Figure 2. Example colour-magnitude diagram for Abell 3084 based on our GMOS and archival *HST*/ACS data. The horizontal dashed line shows the predicted colour of a single stellar population that formed at high redshift and evolved passively to the cluster redshift ($z = 0.22$). The photometric zero point of the GMOS frame was chosen to match the colour of the sequence of massive ($i < 20$) cluster early-type galaxies to this prediction.

3 ANALYSIS AND RESULTS

3.1 Difference images

We normalised each reduced and stacked GMOS frame to an exposure time of one second, and then matched the image quality between visits using the PSFMATCH task in IRAF. The point spread function (PSF) model was empirical and based on 10 isolated, unsaturated, high signal-to-noise ratio stars in the vicinity of the strong-lensing region of each frame. These matched frames were then subtracted from each other in pairs to produce difference images, examples of which are shown in Figures 3 & 4.

The wavelength range of the MUSE datacube ($475 < \lambda < 930$ nm) obtained from our observations of Abell 3084 enables great freedom in the choice of reference image when constructing a difference image. We selected the *HST*/ACS observation through the F606W filter (Section 2.3) as the reference image. We therefore created a F606W pseudo-image from the MUSE datacube for each night upon which we observed Abell 3084, by multiplying the datacubes with the transmission curve of the F606W filter, and integrating under the transmission curve. The difference images were then produced by minimizing residuals in all detected sources, following a similar procedure described by Bacon et al. (2017) in the MUSE observations of the Ultra Deep Field. This optimization is performed over: the Moffat model of the MUSE PSF, a possible astrometric shift between the two images, and the sky background level and average sky transmission. An example difference image is shown in Figure 3.

3.2 Searching for transients in imaging data

We searched the difference images for transient sources both manually and automatically. The manual search was per-

formed by three authors (GPS, MB, AR), and identified no sources consistent with being a point source in the difference images. The only sources found were either residuals from the PSF matching close to the centres of bright galaxies, artefacts related to saturated stars, or a small number of residual bad pixels and cosmic rays. The automated search was performed with SExtractor (Bertin & Arnouts 1996), and found no sources other than PSF matching residuals and artefacts relating to saturated stars.

To calibrate the sensitivity of our GMOS search for candidate transients, we injected fake transients in to the data in the following manner, and attempted to recover them both manually and automatically. We cut out 31×31 pixel stamps from the GMOS data around the same, unsaturated, high signal-to-noise, stars used for the image quality matching. Each injected source was randomly chosen to be one of these bright star stamps, with the flux scaled accordingly, and shot noise added. To test the efficacy of manual recovery, we generated synthetic data sets, each containing (randomly and unknown to those searching) between zero and ten injected sources, with i -band magnitudes drawn uniformly from the range $21 < i < 27$. All injected sources with $i < 25$ were identified by at least two searchers, while no sources with $i > 25$ were identified by anyone. These results were independent of whether sources were injected randomly within 20 arcsec of the brightest cluster galaxy (BCG), or into faint background galaxies (including the spectroscopically confirmed multiply-imaged galaxies) following the methods described by Sharon et al. (2010).

To test the automated search, we generated 10^4 synthetic datasets comprising sources injected at each integer magnitude in the range $21 \leq i \leq 26$. SExtractor was then run on these synthetic data sets, with the source being detected if SExtractor finds a source within 0.5 arcsec of the injected source location. At small angular separations from the BCG (θ_{BCG}) the probability of sources being detected is low due to the residuals in the difference images (Figure 5). The source recovery rate at the very centre (within < 0.5 arcsec of the BCG) is artificially boosted because SExtractor detects the residuals at the centre of the BCG (without an injected source) as a source. However, these scales are generally smaller than the high magnification region close to the radial critical curve, and therefore the residuals at the centre of the BCG are not a major limiting factor in our analysis.

Sources at the typical 5σ point source sensitivity of our GMOS data ($i \simeq 25$) are detected with the expected ~ 80 per cent completeness at $\theta_{\text{BCG}} \gtrsim 5$ arcsec, and sources at $i \simeq 24$ are detectable right down to angular separations of a few arcseconds. We put this in to context by plotting in grey in Figure 5 the solid angle that is magnified by the amount required to reinterpret the strain signal from GW170814 as coming from $z = 0.764$, which is the redshift at which the lens model of Abell 3084 is most robust (Section 2.3), also taking in to account the uncertainty on the luminosity distance to GW170814 at $D_{L,\mu=1} = 540_{-210}^{+130}$ Mpc. The peaks at $\theta_{\text{BCG}} \simeq 4$ arcsec and $\theta_{\text{BCG}} \simeq 12$ arcsec correspond to the radial and tangential critical curves respectively (see the inner and outer red curves in Figure 3). Our search is therefore sensitive at > 80 per cent completeness to point sources at $i \lesssim 24$ that are adjacent to either critical curve and to point sources at $i \lesssim 25$ that are adjacent to the tangential critical

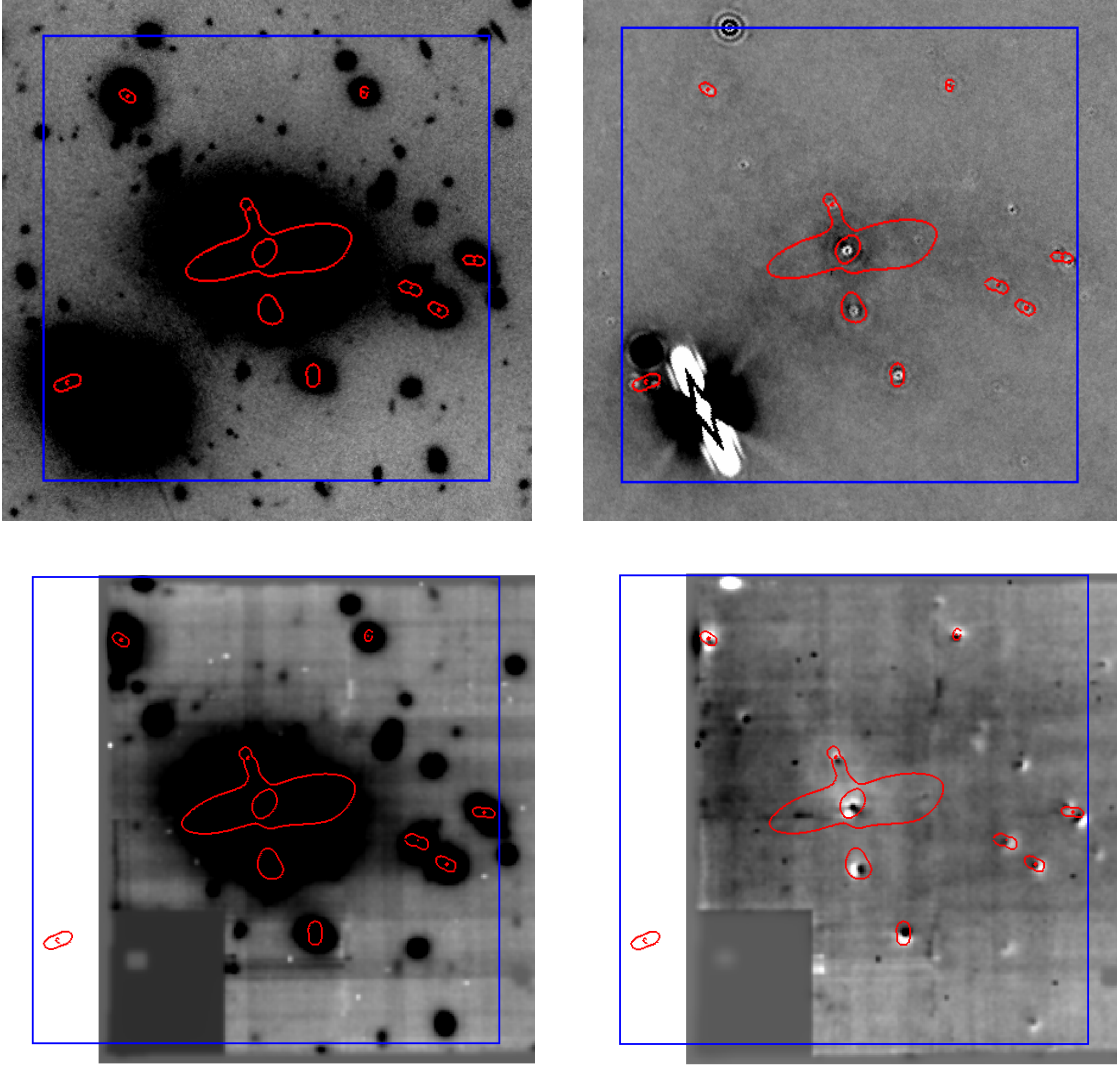


Figure 3. Central 1 arcmin^2 (blue box) of Abell 3084, centred on the brightest cluster galaxy. Examples from our data are shown as follows: GMOS i -band observation (top left); GMOS-based difference image (top right); MUSE observation convolved with the F606W filter (bottom left); MUSE/ HST -based difference image (bottom right). The red curves show the critical curves for $z_S = 0.764$.

curve. We stress that discussion of $z = 0.764$ is by way of example only, and motivated by not wishing to extrapolate the lens model to redshifts at which it is not constrained.

We performed similar manual and automated tests with MUSE images, injecting sources into the inner 15 arcsec of the Abell 3084 MUSE/ HST difference image, obtaining similar results to the GMOS tests described above. Because of the smaller field of view of MUSE compared to GMOS, we did not have a large number of bright stars to use as templates for point sources, but instead used the best-fit Moffat profile discussed in Sec. 2.6. We interpret the slight shortfall in the fraction of fake sources that are recovered from the MUSE/ HST difference images relative to the GMOS images as being caused by the flux sensitivity of the short HST observation being inferior to that of the MUSE observations, after smoothing the HST data to match the ground-based seeing.

3.3 Searching for transients in MUSE data cubes

In addition to the search for continuum sources based on pseudo-images created from the MUSE datacubes, we have performed an automatic search for emission lines across all wavelengths. This is done using the MUSELET detection software, which has been used in the past to automatically search for line emitters in MUSE blank fields (Drake et al. 2017b,a) as well as lensing cluster fields (Mahler et al. 2018; Lagattuta et al. 2017). MUSELET is publicly available as part of the MUSE Python Data Analysis Framework (MPDAF, Conseil et al. 2016) software suite. It is a SExtractor-based detection tool based on a continuum-subtracted datacube where each wavelength plane is replaced by its corresponding narrow-band image, optimised for the detection of typical $\text{FWHM} = 150 \text{ km s}^{-1}$ line width line sources. The sensitivity of MUSELET in recovering point-source line emitters has been extensively tested by Drake et al. (2017a) in the MUSE Ultra Deep Field (Bacon et al. 2017), and we rescale their results to the exposure times of individual dat-

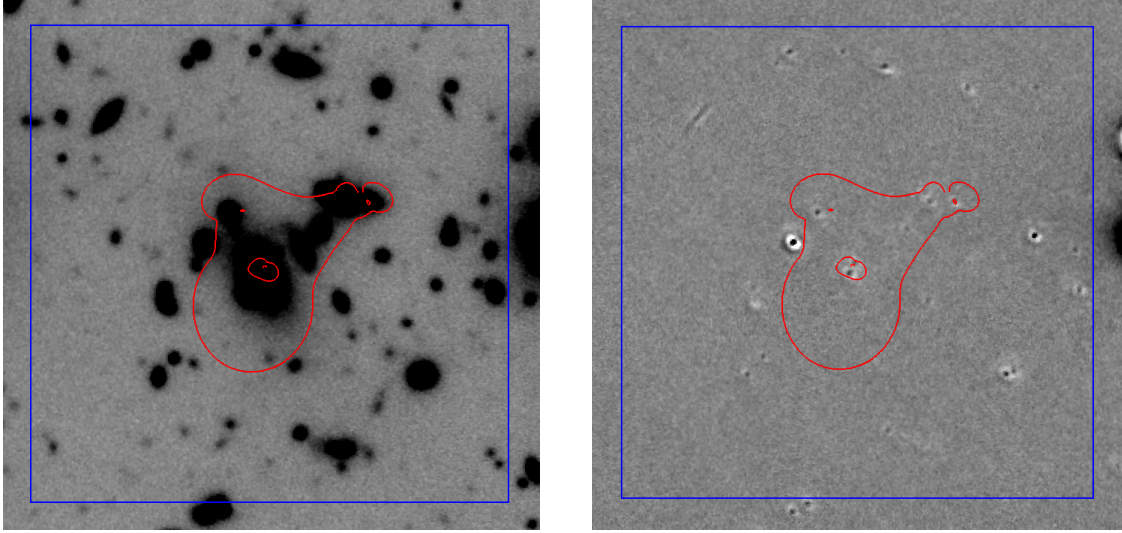


Figure 4. Central 1 arcmin² (blue box) of SMACS J0304.3–4401, centred on the brightest cluster galaxy. Examples from our data are shown as follows: GMOS *i*-band observation (left); GMOS-based difference image (right). The red curve is the tangential critical curve for $z_S = 1.96$.

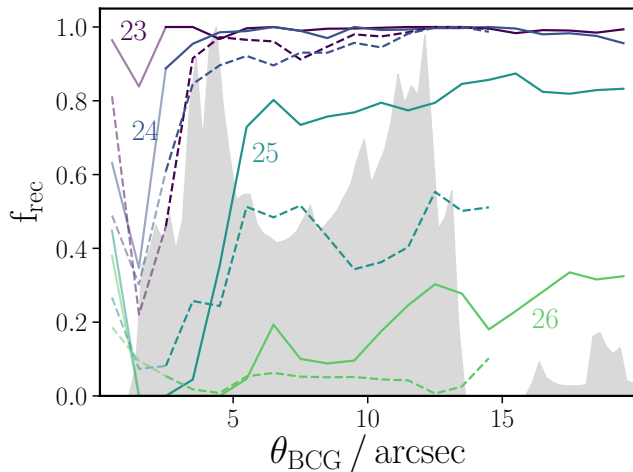


Figure 5. The recovery fraction of injected sources with different *i*-band magnitudes (as labeled), as a function of angular separation from the BCG. The solid lines show fractions for sources injected into GMOS observations of Abell 3084, while the dashed lines are for sources injected into the MUSE/*HST* data for the same cluster. The lines are faded at small radii where the recovery of injected sources is confused by the presence of structured residuals near the BCG centre. The radial distribution of image-plane solid angle magnified sufficiently to reinterpret the LIGO-Virgo detection of GW170814 as originating from $z = 0.764$ is shown by the grey area.

acubes in each night. The values show that our search is complete for line fluxes brighter than $5 \times 10^{-17} \text{ erg s}^{-1} \text{ cm}^{-2}$ (Figure 6).

Removing obvious false detections (sharper than the spatial and/or spectral PSF) through visual inspection, we compare the detection of line emitters found in each datacube as well as the combination of both nights with the reference *HST* image. The only sources appearing as line emitters in MUSE and absent from *HST* are clear Lyman-

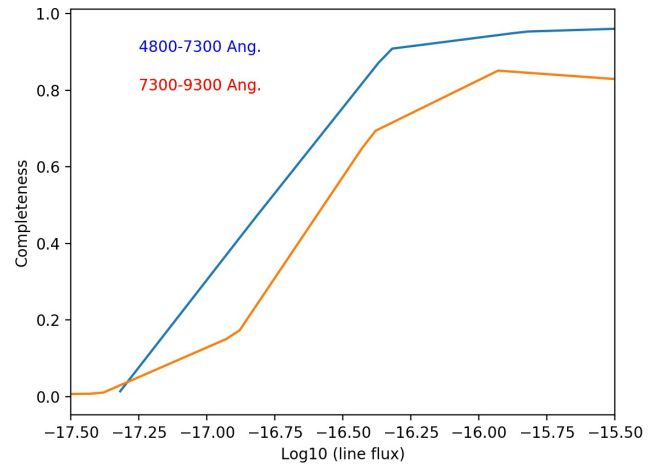


Figure 6. Emission line sensitivity in our search for transients in the individual (per night) MUSE datacubes. Presented is the average completeness level of recovering emission line point sources with MUSELET as a function of line flux, which slightly varies across the cube as a function of the wavelength range.

alpha emitters with strong equivalent width identified from the shape of their spectral lines and/or as multiple images.

4 DISCUSSION

We now discuss the empirical sensitivity of our observations of strong-lensing cluster cores in the context of the plausible EM counterparts to CBC GW sources. We first discuss the cancellation of the inverse square law by lens magnification for strongly-lensed point source EM counterparts to GWs (Section 4.1), and then apply this to kilonova-like EM counterparts (Section 4.2), and EM counterparts that resemble emission from an accretion disk surrounding the product of a BBH merger (Section 4.3).

4.1 Cancellation of the inverse square law by lens magnification

Consider a hypothetical GW source that is inferred by LVC to be at a luminosity distance, $D_{L,\mu=1}$ assuming that it is not gravitationally lensed, i.e. $\mu = 1$, and that has an EM counterpart of absolute magnitude M in an arbitrary pass-band. If this is actually a distant source at $D_{L,\text{true}}$ that is gravitationally magnified by $\mu > 1$, then its apparent magnitude in a pass-band that probes the same rest-frame wavelength range as the pass-band relevant to M (i.e. assuming k -corrections are negligible), is given by:

$$m = M + 5 \log(D_{L,\text{true}}) - 5 - 2.5 \log(\mu), \quad (1)$$

with $D_{L,\text{true}}$ expressed in units of parsecs. As discussed by Smith et al. (2018, and references therein), the interpretation of the strain signal detected by LIGO-Virgo A is degenerate between lens magnification and luminosity distance, $A \propto \mu^{0.5} D_L^{-1}$. Therefore the lens magnification that appears in Equation 1 is given by:

$$\mu = \left(\frac{D_{L,\text{true}}}{D_{L,\mu=1}} \right)^2. \quad (2)$$

The apparent magnitude of the EM counterpart of a lensed GW therefore depends only on the absolute magnitude of the counterpart and the luminosity distance at which the source is placed when (incorrectly) assuming $\mu = 1$:

$$m = M + 5 \log(D_{L,\mu=1}) - 5. \quad (3)$$

The apparent magnitude of a lensed EM counterpart is therefore set by the initial analysis of the signal detected by LIGO-Virgo assuming $\mu = 1$. Therefore observations capable of detecting a given EM counterpart located at $D_{L,\mu=1}$ are also able to detect the same type of counterpart if it is lensed, independent of the true redshift.

4.2 Kilonovae

Optical follow-up observations of BBH sources have so far aimed to achieve the sensitivity required to detect a kilonova at $D_{L,\mu=1}$ (e.g., Soares-Santos et al. 2016; Cowperthwaite et al. 2016; Yoshida et al. 2017; Arcavi et al. 2017; Utsumi et al. 2018). We therefore consider how bright a kilonova counterpart to GW170814 would have been if it had been (formally, regardless of whether or not it had been) lensed. The kilonova counterpart to GW170817 had an absolute magnitude in optical bands of $M \simeq -13.5$ in the few days after discovery (e.g. Arcavi 2018). If GW170814 was strongly-lensed, and had a kilonova-like EM counterpart, then based on $D_{L,\mu=1} = 540_{-210}^{+130}$ Mpc (Section 2.2), it would have an apparent magnitude of $m \simeq 24.1$ – 25.6 independent of its luminosity distance. Our observations reach a depth of $m \simeq 25$ – 26 (Table 1), with a sensitivity to transient sources in our difference image analysis of $m \simeq 24$ – 25 at $\gtrsim 80\%$ completeness. It should therefore have been possible to detect such an EM counterpart if GW170814 was strongly-lensed by one of the clusters that we observed. However, it is highly uncertain whether a BBH source would have a kilonova-like EM counterpart (despite optical follow-up observations, including our own, being designed to detect kilonovae). Kilonova-like emission is more plausible if

GW170814 comprised one or more neutron stars in a BNS or NSBH system.

The primary means of identifying a GW source as a BNS, NSBH or BBH is from the inferred component masses, as neutron stars max a maximum mass of $\lesssim 3 M_\odot$ (Rhoades & Ruffini 1974; Kalogera & Baym 1996; Margalit & Metzger 2017).⁴ For a particular GW signal, the inferred rest-frame mass of the compact objects is inversely proportional to $(1+z)$ where z is the redshift of the GW source. Therefore, the rest-frame mass of GW sources would be revised downwards from the initial estimate by LIGO-Virgo, if they are subsequently identified as being strongly-lensed. The masses of the individual BHs that comprise GW170814 are $30.5_{-3.0}^{+5.7} M_\odot$ and $25.3_{-4.2}^{+2.8} M_\odot$ (Abbott et al. 2017d), i.e. $\gtrsim 8$ times larger than the maximum neutron star mass. Therefore, if GW170814 was strongly-lensed, then it would have to be at $z \gtrsim 7$ to be a credible candidate for having a kilonova-like EM counterpart, which implies a lens magnification of $\mu \simeq 1.7 \times 10^4$. Such high magnifications are possible for point sources located behind galaxy cluster lenses (Miralda-Escude 1991; Diego et al. 2018; Kelly et al. 2018; Rodney et al. 2018). Our observations and difference image analysis yielded no transient sources in the strong-lensing regions of Abell 3084 and SMACS J0304.3–4401 down to $m = 25$. Therefore, if we assume that the rest-frame ultraviolet luminosity of a kilonova-like EM counterpart is similar to the rest-frame optical luminosity of GW170817, we can exclude the interpretation of GW170817 as a BNS or NSBH source at $z > 7$ that has been strongly lensed by either of these clusters.

More generally, our analysis shows that the cancellation of the inverse square law by the degeneracy between luminosity distance and lens magnification has important implications for the EM follow up of GW sources. Specifically, that the detection of EM counterparts to lensed BNS and NSBH sources are within the reach of deep ground-based optical observations with 8-m class telescopes. Our difference image analysis is sensitive to transients as faint as $m \simeq 25$ and are thus sensitive to kilonova-like counterparts to lensed sources that are initially identified at $D_{L,\mu=1} \simeq 500$ Mpc, and independent of their true distance.

In the future, it may be more fruitful to search for lensed optical kilonova-like counterparts to GW sources initially identified as low-mass BBH systems, with individual BH masses of $< 10 M_\odot$, because such lower masses imply a less extreme lens magnification. For example, GW170608 would have been an ideal target for our observing programme, if we had commenced just a few months earlier. GW1706008 comprised (assuming $\mu = 1$) two BHs of masses $12_{-2}^{+7} M_\odot$ and $7_{-2}^{+2} M_\odot$ respectively, at $z = 0.07_{-0.03}^{+0.03}$, which corresponds to $D_{L,\mu=1} = 320_{-140}^{+140}$ Mpc (Abbott et al. 2017c). Following the reasoning outlined above, it is possible that this is a lensed BNS source at $z \simeq 1.5$ – 3.5 , that is magnified by $\mu \simeq 10^3$ – 10^4 . This level of magnification is similar to that suffered by the strongly-lensed individual blue giant star dubbed ‘‘Icarus’’ (Kelly et al. 2018). A kilonova-like coun-

⁴ Neutron stars could also be disambiguated from the imprint of tidal effects on the signal. These are difficult to measure, and could not be conclusively identified for GW170817 despite its high signal-to-noise ratio (Abbott et al. 2017e).

terpart to GW170608 would have an apparent magnitude of $m \simeq 24$ if it is strongly-lensed, independent of its redshift. This is brighter than discussed above for GW170814, but still sufficiently faint to be beyond the reach of most of the current generation of wide-field searches for EM counterparts (Section 2.1).

4.3 Accretion discs

We also consider the possibility of detecting an EM counterpart that is much fainter than a kilonova, and expected to be more plausible as the counterpart to a BBH source. A BBH merger in vacuum is not expected to emit any EM radiation; however, numerous theoretical ideas for EM counterparts to BBH mergers not in vacuum have been proposed following the detection of GW150914 (e.g., Li et al. 2016; Loeb 2016; Lyutikov 2016; Murase et al. 2016; Morsony, Workman & Ryan 2016; Perna, Lazzati & Giacomazzo 2016; Woosley 2016; Yamazaki, Asano & Ohira 2016; Bartos et al. 2017; Dai, McKinney & Miller 2017; de Mink & King 2017; Janiak et al. 2017; Ryan & MacFadyen 2017; Stone, Metzger & Haiman 2017). For illustrative purposes, we adopt a simple model of an EM counterpart and apply Equation 3 for comparison to our results.

We assume that an accretion disc forms around the single BH that forms from the merger of two BHs, that this disc is irradiated by X-ray photons due to accretion of material from the inner disc on to the final BH, and that some of this energy is absorbed by the disc and re-radiated in the rest-frame UV/optical. We adopt the well-studied BH X-ray binary system Cygnus X-1 as the basis for our illustrative calculation. The BH in Cygnus X-1 has a mass of $M_{\text{CygX1}} \simeq 10M_{\odot}$ (Gies & Bolton 1986; Shaposhnikov & Titarchuk 2007), and accretes at ~ 2 per cent of the Eddington limit, independent of its state (Nowak et al. 2012). Estimates of the optical luminosity of the accretion disc have been inferred from variability in the photometry of the companion star, HDE 226868. This variability indicates that the accretion disc contributes ~ 2 –10 per cent of the optical flux of HDE 226868 (Brocksopp et al. 1999), with the upper end of this range plausible at shorter wavelengths, based on the *U*-band photometry. Given that the rest-frame UV emission would be redshifted to the optical bands in which we have observed if the BBH is lensed, we adopt 10 per cent of the optical luminosity of HDE 226868 as the accretion disc luminosity, which corresponds to an absolute magnitude of $M_{\text{CygX1}} \simeq -8 + 2.5 \log(10) = -5.5$.

We further assume that the luminosity of the accretion disc is proportional to the mass of the final BH and the accretion rate as a fraction of the Eddington limit. Therefore, combining these assumptions with the dependence of BH mass on redshift (discussed in Section 1), gives the following expression for the estimated absolute magnitude, M , of the EM counterpart to a lensed BBH merger,

$$M = M_{\text{CygX1}} - 2.5 \log \left(\frac{\lambda}{\lambda_{\text{CygX1}}} \cdot \frac{M_{\text{f},\mu=1}}{M_{\text{CygX1}}} \cdot \frac{1 + z_{\mu=1}}{1 + z} \right), \quad (4)$$

where z is the redshift of the lensed BBH, $M_{\text{f},\mu=1}$ is the final BH mass of a BBH merger inferred assuming $\mu = 1$, and λ denotes accretion rate as a fraction of the Eddington limit, with $\lambda_{\text{CygX1}} \simeq 0.02$, as discussed above.

Substituting Equation 4 in to Equation 3, and adopting

$M_{\text{f},\mu=1} \simeq 53M_{\odot}$, $z_{\mu=1} = 0.11$ for GW170814 (Abbott et al. 2017d), a nominal source redshift of $z \simeq 0.5 - 2$, and $\lambda = 1$, gives $m \simeq 27.4 - 28.2$. This is a factor $\gtrsim 10$ fainter than the transient point sources that we are able to recover in our difference imaging (Section 3.1). This estimate also assumes Eddington limited accretion. A factor of 10 reduction in accretion rate would cause the putative lensed EM counterpart to have an apparent magnitude of $m \simeq 30 - 31$. These faint limits are achievable from space and will be achievable with 30-m class telescopes, and are relevant to lensed BBH sources and their EM counterparts *independent* of the redshift of the lensed source.

5 SUMMARY

In the nights immediately following the announcement of the detection of GW170814, we observed two strong-lensing cluster cores – Abell 3084 and SMACS J0304.3–4401 – identified using the sky localisation available from the LVC. Our observations were conducted with the GMOS and MUSE instruments on the Gemini-South and Very Large Telescope, respectively. The data reach a sensitivity to point sources of $m(5\sigma) \simeq 25 - 26$, and our search for transient sources is sensitive down to $m = 25$ in the continuum and line fluxes of $5 \times 10^{-17} \text{ erg s}^{-1} \text{ cm}^{-2}$. We detect no credible candidate transient sources in the data down to these limits. This is the most sensitive search to date for EM counterparts to GW sources, independent of considerations of possible lens amplification.

We show that lens magnification suffered by a lensed GW source cancels out the inverse square law, and therefore the apparent magnitude of a point source EM counterpart of given luminosity is set by the luminosity distance inferred from the GW data assuming no lens magnification. This has the important implication that the apparent magnitude of EM counterparts to lensed GW sources is independent of the true redshift of the source. We therefore show, as a proof of concept, that we can exclude the idea that GW170814 is a NSBH or BNS source at $z > 7$ that is lensed by either of these clusters. We also discuss how observations with 30-m class telescopes and/or space-based telescopes will be needed to detect lensed EM counterparts to BBH sources whose optical emission is reprocessed emission from an irradiated accretion disc.

In summary, we have confirmed the feasibility of searching for EM counterparts to candidate lensed GW sources with ground-based 8-m class telescopes, and described some important considerations for future development of this new observing strategy within the rapidly growing field of GW astronomy.

ACKNOWLEDGMENTS

We thank the staff and Directors of the Gemini and La Silla Paranal Observatories for their superb support of our observing programmes and awards of Director’s Discretionary time respectively. GPS thanks Olivia Mueller for help and support during August 2017, Iair Arcavi for assistance with Figure 1, and Gary Mamon and colleagues at the Institut d’Astrophysique de Paris for their warm welcome during

the latter stages of writing up this article. We thank Alyssa Drake for providing us with the results of completeness tests to blindly detect line emitters within MUSE datacubes using MUSELET, and Alberto Vecchio for helpful discussions. We acknowledge support from the Science and Technology Facilities Council through the following grants: ST/N000633/1 (GPS, MB, CPLB, WMF); ST/L00075X/1, ST/P000451/1 (MJ); and ST/K005014/1 (JV). JR acknowledges support from the ERC starting grant 336736-CALENDS. RJM acknowledges support from the Royal Society.

REFERENCES

- Abbott B. P. et al., 2016a, *ApJ*, 818, L22
 Abbott B. P. et al., 2016b, *Physical Review X*, 6, 041015
 Abbott B. P. et al., 2016c, *Physical Review Letters*, 116, 061102
 Abbott B. P. et al., 2016d, *Physical Review Letters*, 116, 241102
 Abbott B. P. et al., 2016e, *Living Reviews in Relativity*, 19, 1
 Abbott B. P. et al., 2016f, *Physical Review Letters*, 116, 221101
 Abbott B. P. et al., 2017a, *Nature*, 551, 85
 Abbott B. P. et al., 2017b, *ApJ*, 848, L13
 Abbott B. P. et al., 2017c, *ApJ*, 851, L35
 Abbott B. P. et al., 2017d, *Physical Review Letters*, 119, 141101
 Abbott B. P. et al., 2017e, *Physical Review Letters*, 119, 161101
 Abbott B. P. et al., 2017f, *ApJ*, 848, L12
 Abbott B. P. et al., 2017g, *ApJ*, 850, L40
 Abbott B. P. et al., 2017, *Phys. Rev. Lett.*, 118, 221101
 Ade P. A. R. et al., 2016, *A&A*, 594, A13
 Arcavi I., 2018, *ApJ*, 855, L23
 Arcavi I. et al., 2017, *ApJ*, 848, L33
 Bacon R. et al., 2017, *A&A*, 608, A1
 Bartos I., Kocsis B., Haiman Z., Márka S., 2017, *ApJ*, 835, 165
 Bauswein A., Just O., Janka H.-T., Stergioulas N., 2017, *ApJ*, 850, L34
 Berry C. P. L. et al., 2015, *ApJ*, 804, 114
 Bertin E., Arnouts S., 1996, *A&AS*, 117, 393
 Broadhurst T., Diego J. M., Smoot, III G., 2018, *ArXiv e-prints*
 Brocksopp C., Fender R. P., Larionov V., Lyuty V. M., Tarasov A. E., Pooley G. G., Paciesas W. S., Roche P., 1999, *MNRAS*, 309, 1063
 Bruzual G., Charlot S., 2003, *MNRAS*, 344, 1000
 Chatziioannou K., Yunes N., Cornish N., 2012, *Phys. Rev. D*, 86, 022004
 Christensen L. et al., 2012, *MNRAS*, 427, 1973
 Conseil S., Bacon R., Piqueras L., Shepherd M., 2016, *ArXiv e-prints*
 Coughlin M. W. et al., 2018, *ArXiv e-prints*
 Coulter D. A. et al., 2017, *Science*, 358, 1556
 Cowperthwaite P. S. et al., 2016, *ApJ*, 826, L29
 Dai L., McKinney J. C., Miller M. C., 2017, *MNRAS*, 470, L92
 de Mink S. E., King A., 2017, *ApJ*, 839, L7
 Del Pozzo W., Berry C., Ghosh A., Haines T., Vecchio A., 2018, *ArXiv e-prints*
 Diego J. M. et al., 2018, *ApJ*, 857, 25
 Drake A. B. et al., 2017a, *A&A*, 608, A6
 Drake A. B. et al., 2017b, *MNRAS*, 471, 267
 Fohlmeister J. et al., 2007, *ApJ*, 662, 62
 Gehrels N., Cannizzo J. K., Kanner J., Kasliwal M. M., Nissanke S., Singer L. P., 2016, *ApJ*, 820, 136
 Gies D. R., Bolton C. T., 1986, *ApJS*, 61, 419
 Hanna C., Mandel I., Vousden W., 2014, *ApJ*, 784, 8
 Hilbert S., White S. D. M., Hartlap J., Schneider P., 2008, *MNRAS*, 386, 1845
 Inada N., Oguri M., Rusu C. E., et al., 2014, *AJ*, 147, 153
 Janiak A., Bejger M., Charzyński S., Sukova P., 2017, *New A*, 51, 7
 Kalogera V., Baym G., 1996, *ApJ*, 470, L61
 Kelly P. L. et al., 2018, *Nature Astronomy*, 2, 334
 Krolak A., Schutz B. F., 1987, *General Relativity and Gravitation*, 19, 1163
 Lagattuta D. J. et al., 2017, *MNRAS*, 469, 3946
 Levan A. J. et al., 2017, *ApJ*, 848, L28
 Li S.-S., Mao S., Zhao Y., Lu Y., 2018, *ArXiv e-prints*
 Li X., Zhang F.-W., Yuan Q., Jin Z.-P., Fan Y.-Z., Liu S.-M., Wei D.-M., 2016, *ApJ*, 827, L16
 Liao K., Fan X.-L., Ding X.-H., Biesiada M., Zhu Z.-H., 2017, *ArXiv e-prints*
 LIGO Scientific Collaboration and Virgo Collaboration, 2017a, GRB Coordinates Network, Circular Service, No. 21474, (2017), 21474
 LIGO Scientific Collaboration and Virgo Collaboration, 2017b, GRB Coordinates Network, Circular Service, No. 21474, (2017), 21493
 Loeb A., 2016, *ApJ*, 819, L21
 Lyutikov M., 2016, *ArXiv e-prints*
 Mahler G. et al., 2018, *MNRAS*, 473, 663
 Margalit B., Metzger B. D., 2017, *ApJ*, 850, L19
 Miralda-Escude J., 1991, *ApJ*, 379, 94
 Morsony B. J., Workman J. C., Ryan D. M., 2016, *ApJ*, 825, L24
 Murase K., Kashiyama K., Mészáros P., Shoemaker I., Senno N., 2016, *ApJ*, 822, L9
 Ng K. K. Y., Wong K. W. K., Broadhurst T., Li T. G. F., 2018, *Phys. Rev. D*, 97, 023012
 Nissanke S., Kasliwal M., Georgieva A., 2013, *ApJ*, 767, 124
 Nowak M. A., Wilms J., Hanke M., Pottschmidt K., Markoff S., 2012, *Mem. Soc. Astron. Italiana*, 83, 202
 Oguri M., 2010, *PASJ*, 62, 1017
 Oguri M., Schrabback T., Jullo E., et al., 2013, *MNRAS*, 429, 482
 Pankow C., Chase E. A., Coughlin S., Zevin M., Kalogera V., 2018, *ApJ*, 854, L25
 Perna R., Lazzati D., Giacomazzo B., 2016, *ApJ*, 821, L18
 Rhoades C. E., Ruffini R., 1974, *Physical Review Letters*, 32, 324
 Rodney S. A. et al., 2018, *Nature Astronomy*, 2, 324
 Rodney S. A. et al., 2016, *ApJ*, 820, 50
 Ryan G., MacFadyen A., 2017, *ApJ*, 835, 199
 Shaposhnikov N., Titarchuk L., 2007, *ApJ*, 663, 445
 Sharon K., Bayliss M. B., Dahle H., et al., 2017, *ApJ*, 835, 5
 Sharon K. et al., 2010, *ApJ*, 718, 876

- Singer L. P. et al., 2016, *ApJ*, 829, L15
Singer L. P., Price L. R., 2016, *Phys. Rev. D*, 93, 024013
Singer L. P. et al., 2014, *ApJ*, 795, 105
Smith G. P., Jauzac M., Veitch J., Farr W. M., Massey R.,
Richard J., 2018, *MNRAS*, 475, 3823
Soares-Santos M. et al., 2016, *ApJ*, 823, L33
Soto K. T., Lilly S. J., Bacon R., Richard J., Conseil S.,
2016, *MNRAS*, 458, 3210
Stone N. C., Metzger B. D., Haiman Z., 2017, *MNRAS*,
464, 946
Utsumi Y. et al., 2018, *PASJ*, 70, 1
Veitch J. et al., 2012, *Phys. Rev. D*, 85, 104045
Veitch J. et al., 2015, *Phys. Rev. D*, 91, 042003
Weilbacher P. M., Streicher O., Urrutia T., Pécontal-
Rousset A., Jarno A., Bacon R., 2014, in *Astronomical
Society of the Pacific Conference Series*, Vol. 485, *As-
tronomical Data Analysis Software and Systems XXIII*,
Manset N., Forshay P., eds., p. 451
Wosley S. E., 2016, *ApJ*, 824, L10
Yamazaki R., Asano K., Ohira Y., 2016, *Progress of The-
oretical and Experimental Physics*, 2016, 051E01
Yoshida M. et al., 2017, *PASJ*, 69, 9